Cycle Slips

Detection and Correction Using Inertial Aiding

Malek O. Karaim, Tashfeen B. Karamat, Aboelmagd Noureldin, Mohamed Tamazin, and Mohamed M. Atia

DRUM ROLL PLEASE. The "Innovation" column and *GPS World* are celebrating a birthday. With this issue, we have started the 25th year of publication of the magazine and the column, which appeared in the very first issue and has been a regular feature ever since. Over the years, we have seen many developments in GPS positioning, navigation, and timing with a fair number documented in the pages of this column.

INNOVATION INSIGHTS
with Richard Langley

Cycle slips are a "fly in the ointment."

In January 1990, GPS and GLONASS receivers were still in their infancy. Or perhaps their toddler years. But significant advances in receiver design had already been made since the introduction around 1980 of the first commercially available GPS receiver, the STI-5010, built by Stanford Telecommunications, Inc. It was a dual-frequency, C/A- and P-code, slow-sequencing receiver. Cycling through four satellites took about five minutes, and the receiver unit alone required about 30 centimeters of rack space. By 1990, a number of manufacturers were offering single or dual frequency receivers for positioning, navigation, and timing applications. Already, the first handheld receiver was on the market, the Magellan NAV 1000. Its single sequencing channel could track four satellites. Receiver development has advanced significantly over the intervening 25 years with high-grade multiple frequency, multiple signal, multiple constellation GNSS receivers available from a number of manufacturers, which can record or stream measurements at data rates up to 100 Hz. Consumer-grade receivers have proliferated thanks, in part, to miniaturization of receiver chips and modules. With virtually every cell phone now equipped with GPS, there are over a billion GPS users worldwide. And the chips keep getting smaller. Complete receivers on a chip with an area of less than one centimeter squared are common place. Will the "GPS dot" be in our near future?

The algorithms and methods used to obtain GPS-based positions have evolved over the years, too. By 1990, we already had double-difference carrier-phase processing for precise positioning. But the technique was typically applied in post-processing of collected data. It is still often done that way today. But now, we also have the real-time kinematic (or RTK) technique to achieve similar positioning accuracies in real time and the non-differenced precise point positioning technique, which does not need base stations and which is also being developed for real-time operation. But in all this time, we have always had a "fly in the ointment" when using carrier-phase observations: cycle slips. These are discontinuities in the time series of carrier-phase measurements due to the receiver temporarily losing lock on the carrier of a GPS signal caused by signal blockage, for example. Unless cycle slips are repaired or otherwise dealt with, reduction in positioning accuracy ensues. Scientists and engineers have developed several ways of handling cycle slips not all of which are capable of working in real time. But now, a team of university researchers has developed a technique combining GPS receivers with an inexpensive inertial measuring unit to detect and repair cycle slips with the potential to operate in real time. They describe their system in this month's column.

"Innovation" is a regular feature that discusses advances in GPS technology and its applications as well as the fundamentals of GPS positioning. The column is coordinated by Richard Langley of the Department of Geodesy and Geomatics Engineering, University of New Brunswick. He welcomes comments and topic ideas. To contact him, see the "Contributing Editors" section on page 4.

GPS carrier-phase measurements can be used to achieve very precise positioning solutions. Carrier-phase measurements are much more precise than pseudorange measurements, but they are ambiguous by an integer number of cycles. When these ambiguities are resolved, sub-centimeter levels of positioning can be achieved.

However, in real-time kinematic applications, GPS signals could be lost temporarily because of various disturbing factors such as blockage by trees, buildings, and bridges and by vehicle dynamics. Such signal loss causes a discontinuity of the integer number of cycles in the measured carrier phase, known as a cycle slip. Consequently, the integer counter is reinitialized, meaning that the integer ambiguities become unknown again. In this event, ambiguities need to be resolved once more to resume the precise positioning and navigation process. This is a computation-intensive and time-consuming task. Typically, it takes at least a few minutes to resolve the ambiguities.

The ambiguity resolution is even more challenging in real-time navigation due to receiver dynamics and the time-sensitive nature of the required kinematic solution. Therefore, it would save effort and time if we could detect and estimate the size of these cycle slips and correct the measurements accordingly instead of resorting to a new ambiguity resolution. In this article, we will briefly review the cause of cycle slips and present a procedure for detecting and correcting cycle slips using a tightly coupled GPS/inertial system, which could be used in real time. We will also discuss practical tests of the procedure.

Cycle Slips and Their Management

A cycle slip causes a jump in carrier-phase measurements when the receiver phase tracking loops experience a temporary

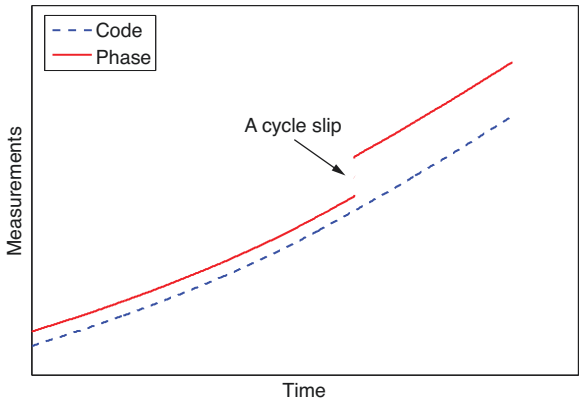

▲ **FIGURE 1** A cycle slip affecting phase measurements but not the pseudoranges.

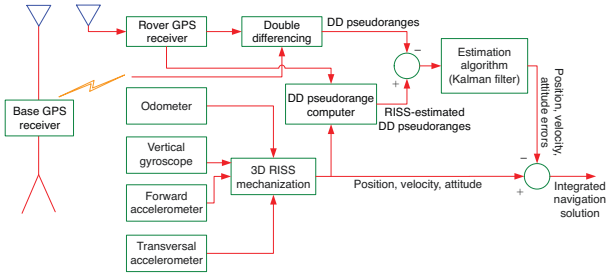

▲ **FIGURE 3** Tightly coupled integration of GPS/RISS using differential pseudorange measurements.

loss of lock due to signal blockage or some other disturbing factor. On the other hand, pseudoranges remain unaffected. This is graphically depicted in FIGURE 1. When a cycle slip happens, the Doppler (cycle) counter in the receiver restarts, causing a jump in the instantaneous accumulated phase by an integer number of cycles. Thus, the integer counter is reinitialized, meaning that ambiguities are unknown again, producing a sudden change in the carrier-phase observations.

Once a cycle slip is detected, it can be handled in two ways. One way is to repair the slip. The other way is to reinitialize the unknown ambiguity parameter in the phase measurements. The former technique requires an exact estimation of the size of the slip but could be done instantaneously. The latter solution is more secure, but it is time-consuming and computationally intensive. In our work, we follow the first approach, providing a real-time cycle-slip detection and correction algorithm based on a GPS/inertial integration scheme.

GPS/INS Integration

An inertial navigation system (INS) can provide a smoother and more continuous navigation solution at higher data rates than a GPS-only system, since it is autonomous and immune to the kinds of interference that can deteriorate GPS positioning quality. However, INS errors grow with time due to the inherent mathematical double integration in the mechanization process. Thus, both GPS and INS systems exhibit mutually complementary characteristics, and their integration provides a more accurate and robust navigation solution than either stand-alone system. GPS/INS integration is often implemented using a filtering technique. A Kalman filter is typically selected for its

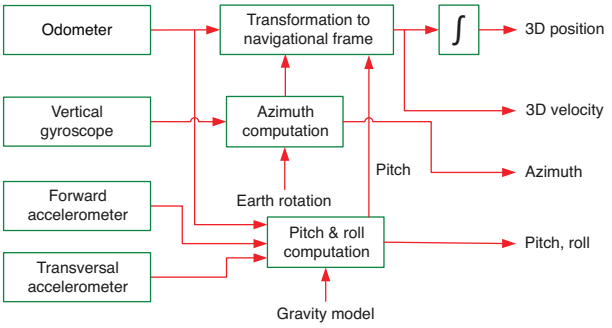

▲ **FIGURE 2** A general view of the RISS configuration.

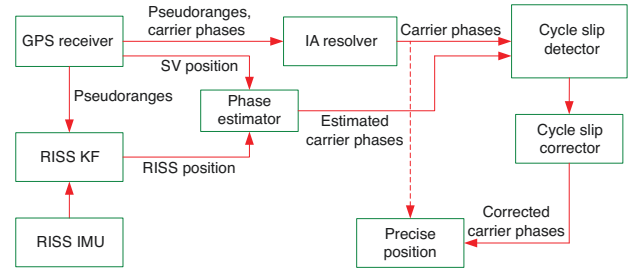

▲ **FIGURE 4** The general flow diagram of the proposed algorithm.

estimation optimality and time-recursion properties.

The two major approaches of GPS/INS integration are loosely coupled and tightly coupled. The former strategy is simpler and easier to implement because the inertial and GPS navigation solutions are generated independently before being weighted together by the Kalman filter. There are two main drawbacks with this approach: 1) signals from at least four satellites are needed for a navigation solution, which cannot always be guaranteed; and 2) the outputs of the GPS Kalman filter are time correlated, which has a negative impact upon the system performance. The latter strategy performs the INS/GPS integration in a single centralized Kalman filter. This architecture eliminates the problem of correlated measurements, which arises due to the cascaded Kalman filtering in the loosely coupled approach. Moreover, the restriction of visibility of at least four satellites is removed. We specifically use a tightly coupled GPS/reduced inertial sensor system approach.

Reduced Inertial Sensor System. Recently, microelectromechanical system or MEMS-grade inertial sensors have been introduced for low-cost navigation applications. However, these inexpensive sensors have complex error characteristics. Therefore, current research is directed towards the utilization of fewer numbers of inertial sensors inside the inertial measurement unit (IMU) to obtain the navigation solution.

The advantage of this trend is twofold. The first is avoidance of the effect of inertial sensor errors. The second is reduction of the cost of the IMU in general. One such minimization approach, and the one used in our work, is known as the reduced inertial sensor system (RISS). The RISS configuration uses one gyroscope, two accelerometers, and a vehicle wheel-rotation sensor. The gyroscope is used to observe the changes in the vehicle's orientation in the horizontal plane. The two accelerometers are used to obtain the pitch and roll angles. The wheel-rotation sensor

readings provide the vehicle's speed in the forward direction. FIGURE 2 shows a general view of the RISS configuration.

A block diagram of the tightly coupled GPS/RISS used in our work is shown in FIGURE 3. At this stage, the system uses GPS pseudoranges together with the RISS observables to compute an integrated navigation solution. In this three-dimensional (3D) version of RISS, the system has a total of nine states. These states are the latitude, longitude, and altitude errors $(\delta\varphi, \delta\lambda, \delta h)$; the east, north, and up velocity errors $(\delta v_e, \delta v_n, \delta v_u)$; the azimuth error (δA); the error associated with odometer-driven acceleration (δa_{od}); and the gyroscope error $(\delta\omega_z)$.

The nine-state error vector $\boldsymbol{x}_k$ at time t_k is expressed as:

$$\boldsymbol{x}_k = (\delta\phi, \delta\lambda, \delta h, \delta v_e, \delta v_n, \delta v_u, \delta A, \delta a_{od}, \delta\omega_z) \quad (1)$$

Cycle Slip Detection and Correction

Cycle slip handling usually happens in two discrete steps: detection and fixing or correction. In the first step, using some testing quantity, the location (or time) of the slip is found. During the second step, the size of the slip is determined, which is needed along with its location to fix the cycle slip. Various techniques have been introduced by researchers to address the problem of cycle-slip detection and correction. Different measurements and their combinations are used including carrier phase minus code (using L1 or L2 measurements), carrier phase on L1 minus carrier phase on L2, Doppler (on L1 or L2), and time-differenced phases (using L1 or L2). In GPS/INS integration systems, the INS is used to predict the required variable to test for a cycle slip, which is usually the true receiver-to-satellite range in double-difference (DD) mode, differencing measurements between a reference receiver and the roving receiver and between satellites. In this article, we introduce a tightly coupled GPS/RISS approach for cycle-slip detection and correction, principally for land vehicle navigation using a relative-positioning technique.

Principle of the Algorithm. The proposed algorithm compares DD L1 carrier-phase measurements with estimated values derived from the output of the GPS/RISS system. In the case of a cycle slip, the measurements are corrected with the calculated difference. A general overview of the system is given in FIGURE 4.

The number of slipped cycles $\delta N(t)$ is given by

$$\delta N(t) = \Delta\nabla\phi(t) - \Delta\nabla\hat{\phi}(t) \quad (2)$$

where

$\Delta\nabla\phi(t)$ is the DD carrier-phase measurement (in cycles)

$\Delta\nabla\hat{\phi}(t)$ is DD estimated carrier phase value (in cycles).

$\delta N(t)$ is compared to a pre-defined threshold μ. If the threshold is exceeded, it indicates that there is a cycle slip in the DD carrier-phase measurements. Theoretically, $\delta N(t)$ would be an integer but because of the errors in the measured carrier phase as well as errors in the estimations coming from the INS system, $\delta N(t)$ will be a real or floating-point number.

The estimated carrier-phase term in Equation (2) is obtained as follows:

$$\Delta\nabla\hat{\phi}(t) = \frac{1}{\lambda}\left\{\left[\hat{r}_{\mathrm{R}}^{i}(t) - r_{\mathrm{B}}^{i}(t)\right] - \left[\hat{r}_{\mathrm{R}}^{j}(t) - r_{\mathrm{B}}^{j}(t)\right]\right\} \quad (3)$$

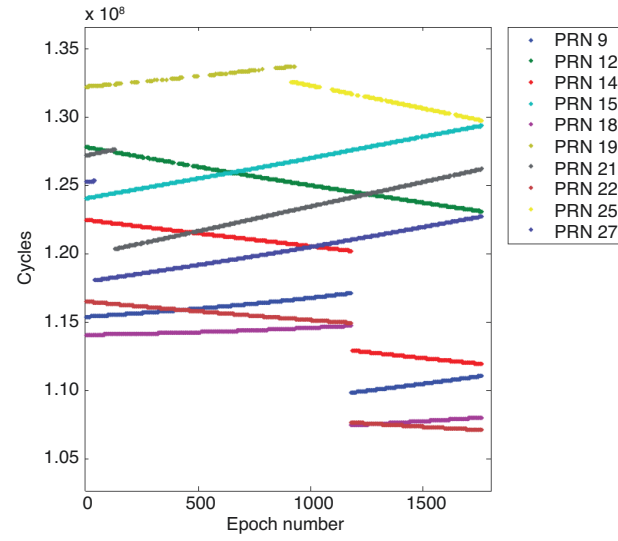

▲ **FIGURE 5** Measured carrier phase at the rover.

where

λ is the wavelength of the signal carrier (in meters)

$\hat{r}_{\mathrm{R}}^{i}(t), \hat{r}_{\mathrm{R}}^{j}(t)$ are the estimated ranges from the rover to satellites *i* and *j* respectively (in meters)

$r_{\mathrm{B}}^{i}(t), r_{\mathrm{B}}^{j}(t)$ are known ranges from the base to satellites *i* and *j* respectively (in meters).

What we need to get from the integrated GPS/RISS system is the estimated range vector from the receiver to each available satellite $(\hat{r}_R^1, \hat{r}_R^2, \cdots, \hat{r}_R^m)$. Knowing our best position estimate, we can calculate ranges from the receiver to all available satellites through:

$$\hat{\boldsymbol{r}}_{\mathrm{R}}^{m} = \left\| \boldsymbol{x}^{\mathrm{KF}} - \boldsymbol{x}^{m} \right\|, \; m = 1, \ldots, M \quad (4)$$

where

$\hat{\boldsymbol{r}}_{\mathrm{R}}^{m}$ is the calculated range from the receiver to the *m*th satellite

$\boldsymbol{x}^{\mathrm{KF}}$ is the receiver position obtained from GPS/RISS Kalman filter solution

$\boldsymbol{x}^{m}$ is the position of the *m*th satellite

M is the number of available satellites.

Then, the estimated DD carrier-phase term in Equation (3) can be calculated and the following test quantity in Equation (2) can be applied:

$$\delta N^{i}(t) = \Delta\nabla\phi^{i}(t) - \Delta\nabla\hat{\phi}^{i}(t), \quad i = 1, \ldots, M-1 \quad (5)$$

If a cycle slip occurred in the *i*th DD carrier-phase set, the corresponding set is instantly corrected for that slip by:

$$\Delta\nabla\phi^{s}(t) = \Delta\nabla\phi^{s}(t) - \delta N^{i}(t) \quad (6)$$

where *s* is the DD carrier-phase-set number in which the cycle slip has occurred.

Experimental Work

The performance of the proposed algorithm was examined on the data collected from several real land-vehicle trajectories. A high-end tactical grade IMU was integrated with a survey-grade GPS receiver to provide the reference solution. This IMU uses three ring-laser gyroscopes and three accelerometers mounted orthogonally to measure angular rate and linear acceleration. The GPS receiver and the IMU were integrated in a commercial package. For the GPS/RISS solution, the same GPS receiver

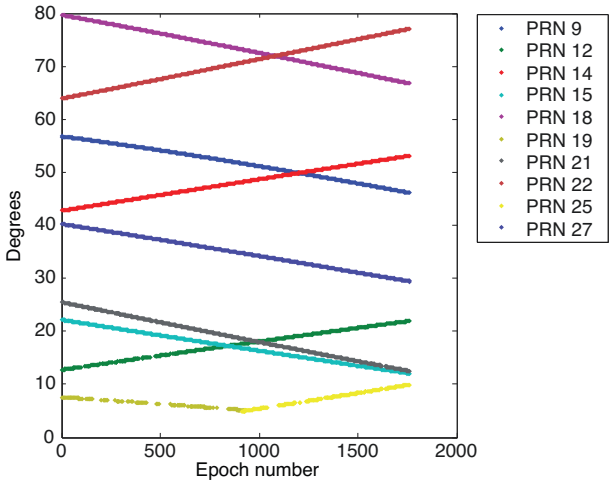

▲ **FIGURE 6** Satellite elevation angles.

	MEMS IMU	Tactical Grade IMU
Size	7.62 × 9.53 × 8.13 (cm)	16 × 16 × 10 (cm)
Mass	0.59 kg	0.725 kg
Max. data rate	200 Hz	100 Hz
Gyroscope		
Range	± 100 °/s	± 1000 °/s
Bias	< ± 2.0 °/s	1 °/hr
Scale factor	< 1 %	150 ppm
Random walk	< 2.25 °/$\sqrt{hr}$	< 0.125 °/$\sqrt{hr}$
Accelerometer		
Range	± 2 g	± 50 g
Bias	± 30 mg	1.0 mg
Scale factor	< 1 %	300 ppm
Random walk	< 0.15 m/s/$\sqrt{hr}$	< 0.198 m/s/$\sqrt{hr}$

▲ **TABLE 1** Characteristics of the MEMS and tactical grade IMUs.

and a MEMS-grade IMU were used. This IMU is a six-degree of freedom inertial system, but data from only the vertical gyroscope, the forward accelerometer, and the transversal accelerometer was used. TABLE 1 gives the main characteristics of both IMUs. The odometer data was collected using a commercial data logger through an On-Board Diagnostics version II (OBD-II) interface. Another GPS receiver of the same type was used for the base station measurements. The GPS data was logged at 1 Hz.

Several road trajectories were driven using the above-described configuration. We have selected one of the trajectories, which covers several real-life scenarios encountered in a typical road journey, to show the performance of the proposed algorithm. The test was carried out in the city of Kingston, Ontario, Canada. The starting and end point of the trajectory was near a well-surveyed point at Fort Henry National Historic Site where the base station receiver was located. The length of the trajectory was about 30 minutes, and the total distance traveled was about 33 kilometers with a maximum baseline length of about 15 kilometers. The trajectory incorporated a portion of Highway 401 with a maximum speed limit of 100 kilometers per hour and

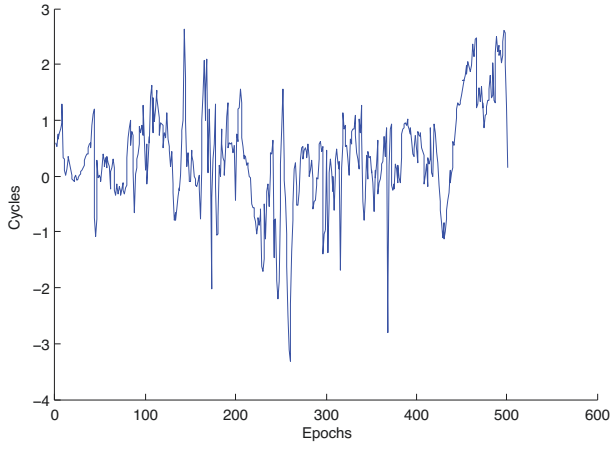

▲ **FIGURE 7** DD-carrier-phase estimation error, reference satellite with PRN 22.

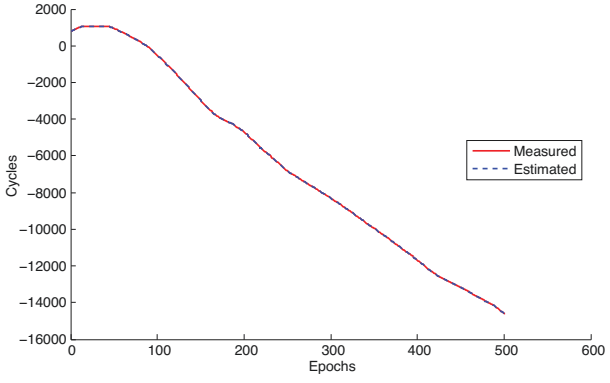

▲ **FIGURE 8** Measured versus estimated DD carrier phase, reference satellite with PRN 22.

suburban areas with a maximum speed limit of 80 kilometers per hour. It also included different scenarios including sharp turns, high speeds, and slopes.

FIGURE 5 shows measured carrier phases at the rover for the different satellites. Some satellites show very poor presence whereas some others are consistently available. Satellites elevation angles can be seen in FIGURE 6.

Results

We start by showing some results of carrier-phase estimation errors. Processing is done on what is considered to be a cycle-slip-free portion of the data set for some persistent satellites (usually with moderate to high elevation angles). Then we show results for the cycle-slip-detection process by artificially introducing cycle slips in different scenarios. In the ensuing discussion (including tables and figures), we show results indicating satellite numbers without any mention of reference satellites, which should be implicit as we are dealing with DD data.

FIGURE 7 shows DD carrier-phase estimation errors whereas FIGURE 8 shows DD measured carrier phases versus DD estimated carrier phases for sample satellite PRN 22. As can be seen in TABLE 2, the root-mean-square (RMS) error varies from 0.93 to 3.58 cycles with standard deviations from 0.85 to 2.47 cycles. Estimated phases are approximately identical to the measured ones. Nevertheless, most of the DD carrier-phase estimates have

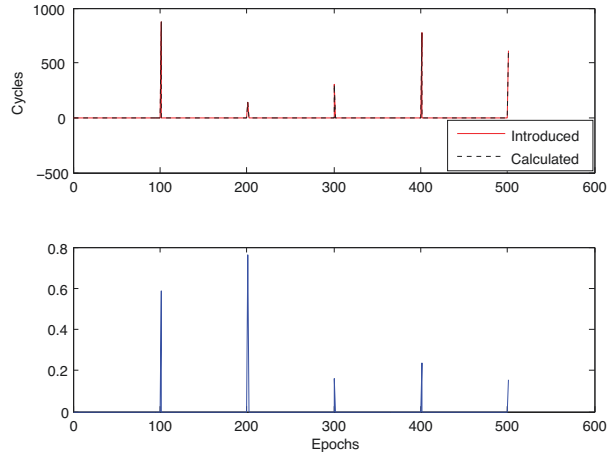

▲ **FIGURE 9** Introduced and calculated cycle slips (upper plot) and detection error (lower plot). Few cycle slips case, reference satellite with PRN 22.

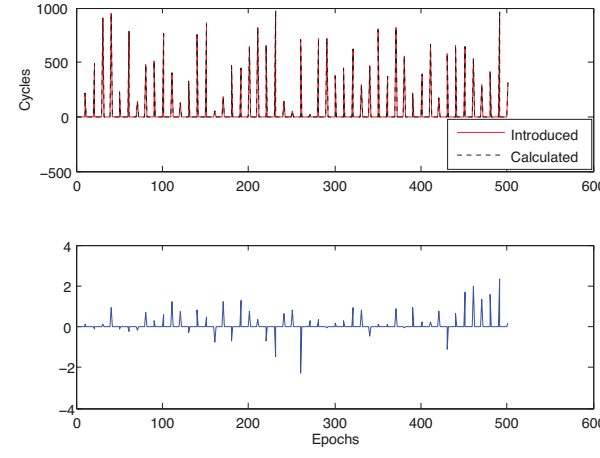

▲ **FIGURE 10** Introduced and calculated cycle slips (upper plot) and detection error (lower plot). Moderate cycle slips case, reference satellite with PRN 22.

bias and general drift trends, which need some elaboration. In fact, the bias error can be the result of more than one cause. The low-cost inertial sensors always have bias in their characteristics, which plays a major role in this. The drift is further affecting relatively lower elevation angle satellites which can also be attributed to more than one reason. Indeed, one reason for choosing this specific trajectory, which was conducted in 2011, was to test the algorithm with severe ionospheric conditions as the year 2011 was close to a solar maximum: a period of peak solar activity in the approximately 11-year sunspot cycle.

Moreover, the time of the test was in the afternoon, which has the maximum ionospheric effects during the day. Thus, most part of the drift trend must be coming from ionospheric effects as the rover is moving away from the base receiver during this portion of the trajectory. Furthermore, satellite geometry could contribute to this error component. Most of the sudden jumps coincide with, or follow, sharp vehicle turns and rapid tilts. Table 2 shows the averaged RMS and standard deviation (std) DD carrier-phase estimation error for the sample satellite-pairs. We introduced cycle slips at different rates or intensities and different sizes to simulate real-life scenarios. Fortunately, cycle slips are usually big as mentioned earlier and this was corroborated by our observations from real trajectory data. Therefore, it is more important to detect and correct for bigger slips in general.

Introducing and Detecting Cycle Slips. To test the robustness of the algorithm, we started with an adequate cycle slip size. Cycle slips of size 10–1000 cycles were introduced with different intensities. These intensities are categorized as few (1 slip per 100 epochs), moderate (10 slips per 100 epochs), and severe (100 slips per 100 epochs). This was applied for all DD carrier-phase measurement sets simultaneously. The threshold was set to 1.9267 (average of RMS error for all satellite-pairs) cycles. Four metrics were used to describe the results. Mean square error (MSE); accuracy, the detected cycle slip size with respect to the introduced size; True detection (TD) ratio; and Mis-detection (MD) ratio. Due to space constraints and the similarity between results for different satellites, we only show results for the reference satellite with PRN 22. FIGURES 9–12 show introduced versus calculated cycle slips along with the corresponding detection error for sample satellites in the different scenarios. TABLES 3–5 summarize these results.

All introduced cycle slips were successfully detected in all of the few, moderate, and severe cases with very high accuracy. A slight change in the accuracy (increasing with higher intensity) among the different scenarios shows that detection accuracy is not affected by cycle-slip intensity. Higher mis-detection ratios for smaller cycle-slip intensity comes from bigger error margins than the threshold for several satellite pairs. However, this is not affecting the overall accuracy strongly as all mis-detected slips are of comparably very small sizes. MD ratio is zero in the intensive cycle-slip case as all epochs contain slips is an indicator of performance compromise with slip intensity.

It is less likely to have very small cycle

Satellite pair	RMS (cycles)	Std (cycles)
Ref-PRN 9	1.15	0.85
Ref-PRN 14	1.45	1.38
Ref-PRN 18	3.58	2.47
Ref-PRN 22	0.93	0.87
Ref-PRN 27	2.49	1.86
Average	1.93	1.49

▲ **TABLE 2** Estimation error for DD carrier phases (in cycles)

Satellite pair	Accuracy (%)	TD (%)	MD (%)	MSE (cycles)
Ref-PRN 9	99.72	100	93.75	.014
Ref-PRN 14	99.85	100	96.03	.008
Ref-PRN 15	99.14	100	98.61	.156
Ref-PRN 22	99.90	100	91.07	.002
Ref-PRN 27	99.40	100	98.16	.066
Average	99.60	100	95.50	.049

▲ **TABLE 3** Few slips (1 slip per 100 epochs)

Satellite pair	Accuracy (%)	TD (%)	MD (%)	MSE (cycles)
Ref-PRN 9	99.83	100	58.33	0.127
Ref-PRN 14	99.89	100	68.55	0.194
Ref-PRN 15	99.51	100	86.59	1.237
Ref-PRN 22	99.92	100	48.45	0.082
Ref-PRN 27	99.65	100	82.87	0.600
Average	99.76	100	68.59	0.448

▲ **TABLE 4** Moderate slips (10 slips per 100 epochs)

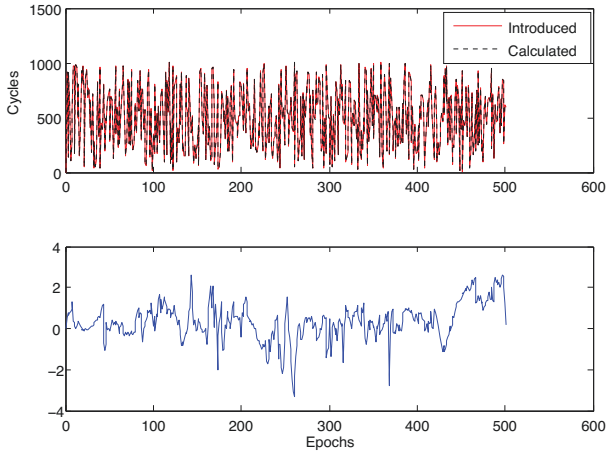

▲ **FIGURE 11** Introduced and calculated cycle slips (upper plot) and detection error (lower plot). Intensive cycle slips case, reference satellite with PRN 22.

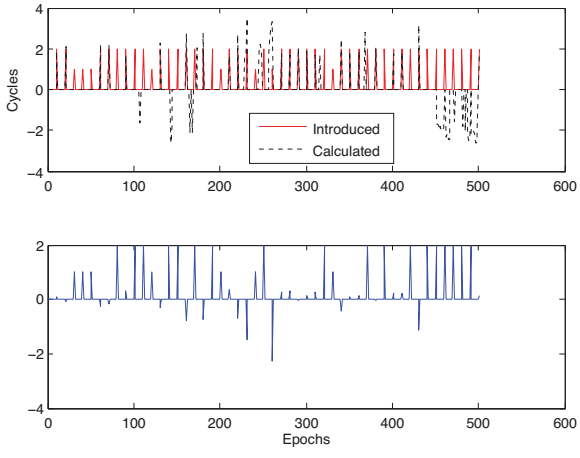

▲ **FIGURE 12** Introduced and calculated cycle slips (upper plot) and detection error (lower plot). Small cycle slips case, reference satellite with PRN 22.

Satellite pair	Accuracy (%)	TD (%)	MD (%)	MSE (cycles)
Ref-PRN 9	99.84	100	0	1.335
Ref-PRN 14	99.90	100	0	2.122
Ref-PRN 15	99.52	100	0.199	12.816
Ref-PRN 22	99.93	100	0	0.880
Ref-PRN 27	99.65	100	0	6.242
Average	99.76	100	0.039	4.679

▲ **TABLE 5** Intensive slips (100 slips per 100 epochs)

Satellite pair	Accuracy (%)	TD (%)	MD (%)	MSE (cycles)
Ref-PRN 9	26.75	22	86.41	0.268
Ref-PRN 14	63.04	50	81.34	0.222
Ref-PRN 15	31.46	48	90.08	1.202
Ref-PRN 22	56.65	46	67.14	0.190
Ref-PRN 27	6.44	34	93.43	0.562
Average	36.86	40	83.68	0.488

▲ **TABLE 6** Small slips (1–2 cycles) at moderate intensity (10 slips per 100 epochs)

slips (such as 1 to 2 cycles) in the data and usually it will be hidden with the higher noise levels in kinematic navigation with low-cost equipment. However, we wanted to show the accuracy of detection in this case. We chose the moderate cycle slip intensity for this test. TABLE 6 summarizes results for all satellites.

We get a moderate detection ratio and modest accuracy as the slips are of sizes close to the threshold. The MSE values are not far away from the case of big cycle slips but with higher mis-detection ratio.

Conclusions

The performance of the proposed algorithm was examined on several real-life land vehicle trajectories, which included various driving scenarios including high and slow speeds, sudden accelerations, sharp turns and steep slopes. The road testing was designed to demonstrate the effectiveness of the proposed algorithm in different scenarios such as intensive and variable-sized cycle slips.

Results of testing the proposed method showed competitive detection rates and accuracies comparable to existing algorithms that use full MEMS IMUs. Thus with a lower cost GPS/RISS integrated system, we were able to obtain a reliable phase-measurement-based navigation solution. Although the testing discussed in this article involved post-processing of the actual collected data at the reference station and the rover, the procedure has been designed to work in real time where the measurements made at the reference station are transmitted to the rover via a radio link. This research has a direct influence on navigation in real-time applications where frequent cycle slips occur and resolving integer ambiguities is not affordable because of time and computational reasons and where system cost is an important factor.

Acknowledgments

This article is based on the paper "Real-time Cycle-slip Detection and Correction for Land Vehicle Navigation using Inertial Aiding" presented at ION GNSS+ 2013, the 26th International Technical Meeting of the Satellite Division of The Institute of Navigation held in Nashville, Tennessee, September 16–20, 2013.

Manufacturers

The research reported in this article used a **Honeywell Aerospace** (*aerospace.honeywell.com*) HG1700 AG11 tactical-grade IMU and a **NovAtel** (*www.novatel.ca*) OEM4 GPS receiver integrated in a NovAtel G2 Pro-Pack SPAN unit, a **Crossbow Technology** (now Moog Crossbow, *www.xbow.com*) IMU300CC MEMS-grade IMU, an additional NovAtel OEM4 receiver at the base station, a pair of NovAtel GPS-702L antennas, and a **Davis Instruments** (*www.davisnet.com*) CarChip E/X 8225 OBD-II data logger.

MALEK KARAIM is a Ph.D. student in the Department of Electrical and Computer Engineering of Queen's University, Kingston, Ontario, Canada.

TASHFEEN KARAMAT is a doctoral candidate in the Department of Electrical and Computer Engineering at Queen's University.

ABOELMAGD NOURELDIN is a cross-appointment professor in the Departments of Electrical and Computer Engineering at both Queen's University and the Royal Military College (RMC) of Canada, also in Kingston.

MOHAMED TAMAZIN is a Ph.D. student in the Department of Electrical and Computer Engineering at Queen's University and a member of the Queen's/RMC NavINST Laboratory.

MOHAMED M. ATIA is a research associate and deputy director of the Queen's/RMC NavINST Laboratory.

MORE ONLINE

Further Reading

For references related to this article, go to *gpsworld.com* and click on *Innovation* in the navigation bar.